Development of Xe and Kr empirical potentials for CeO$_2$, ThO$_2$, UO$_2$ and PuO$_2$, combining DFT with high temperature MD

M W D Cooper[1], N Kuganathan[2], P A Burr[3], M J D Rushton[2], R W Grimes[2], C R Stanek[1] and D A Andersson[1]

[1] Materials Science and Technology Division, Los Alamos National Laboratory, PO Box 1663, Los Alamos, NM 87545, USA
[2] Department of Materials, Imperial College London, London, SW7 2AZ, UK
[3] School of Electrical Engineering and Telecommunications, University of New South Wales, Kensington, 2052, NSW, Australia

E-mail: cooper_m@lanl.gov

Abstract

The development of embedded atom method (EAM) many-body potentials for actinide oxides and associated mixed oxide (MOX) systems has motivated the development of a complementary parameter set for gas-actinide and gas-oxygen interactions. A comprehensive set of density functional theory (DFT) calculations were used to study Xe and Kr incorporation at a number of sites in CeO$_2$, ThO$_2$, UO$_2$ and PuO$_2$. These structures were used to fit a potential, which was used to generate molecular dynamics (MD) configurations incorporating Xe and Kr at 300 K, 1500 K, 3000 K and 5000 K. Subsequent matching to the forces predicted by DFT for these MD configurations was used to refine the potential set. This fitting approach ensured weighted fitting to configurations that are thermodynamically significant over a broad temperature range, while avoiding computationally expensive DFT-MD calculations. The resultant gas potentials were validated against DFT trapping energies and are suitable for simulating combinations of Xe and Kr in solid solutions of CeO$_2$, ThO$_2$, UO$_2$ and PuO$_2$, providing a powerful tool for the atomistic simulation of conventional nuclear reactor fuel UO$_2$ as well as advanced MOX fuels.

Keywords: molecular dynamics, empirical potentials, atomic interactions, fission gas, nuclear fuel

(Some figures may appear in colour only in the online journal)

1. Introduction

The pre-eminent nuclear fuel has been UO$_2$ for several decades due to its radiation tolerance, high melting point and ability to accommodate the significant chemical changes experienced during reactor operation [1]. A particular problem for nuclear fuel is the release of the fission gases Xe and Kr from the pellet and into the helium-filled clad-pellet gap. This has the combined effect of reducing thermal conductivity and increasing the pressure of the plenum or cladding [2]. Other than causing an increased risk of centerline pellet melting, the

high temperatures arising due to poor gap thermal conductivity also give rise to higher mobility and additional release of fission gases [3–5], further exacerbating the problem. A mitigating factor could be an increase in pellet thermal conductivity as the concentration of fission gas in solution in UO$_2$ is reduced [6]. Nonetheless, an eventual consequence of continued fission gas release is the rupturing of the cladding material and this represents a very real problem for nuclear reactor operation. An additional complexity arises during burn-up as U is transmuted to other actinides, in particular Pu^{239}. Alternatively, PuO$_2$ [7, 8] or ThO$_2$ [9] can be blended with UO$_2$ to form MOX

fuels. It is, therefore, important to consider how such changes to the host lattice could alter fission gas behaviour and impact fuel performance. The use of Ce as a surrogate for Pu [10] or U [11] means CeO$_2$ is also of interest.

The underlying mechanisms for fission gas behaviour, as discussed, are complex and inter-related, whereby the temperature and radiation flux in the pellet have important effects [12]. There has been a strong focus on investigating the impact of fission gas on thermal conductivity [6], fission gas mobility in the bulk lattice or at extended defects [3–5, 13, 14] and the behaviour of fission gas bubbles [15–17]. By understanding and predicting these processes over a range of conditions, in particular a large temperature range, a greater understanding of fuel behaviour can be achieved. However, the accuracy of atomic scale simulations is underpinned by the models and theories upon which they are based. In particular, MD simulations are highly dependent upon the ability of a parameter set to accurately describe the properties of both the host UO$_2$ (or MOX) and the interaction of fission gas with the host lattice. Previously, Cooper, Rushton and Grimes (CRG) developed a many-body potential for pure actinide oxides and their mixed oxides [18–20]. The potential is capable of accurately predicting a large number of the thermophysical properties of these systems from 300 K to 3000 K. In particular, this is the first instance of an empirical potential being able to reproduce the bulk modulus of UO$_2$ from 300 K to 3000 K. Here we build upon this work by developing potentials for gas-oxygen and gas-actinide interactions that are consistent with this many-body actinide oxide potential set and that will enable the behaviour of fission gases in mixed oxides to be investigated. A combined classical MD and DFT force matching fitting approach will be presented. The new model is validated against literature and newly presented DFT defect trapping energies for Xe and Kr in CeO$_2$, ThO$_2$, UO$_2$ and PuO$_2$.

2. Methodology

2.1. Potential model

MD simulations, employing a set of interatomic potentials for CeO$_2$, ThO$_2$, UO$_2$ and CeO$_2$ derived previously [18–20][4], are carried out using the large-scale atomic/molecular massively parallel simulator (LAMMPS) [22]. In this model the potential energy, E_i, of an atom i with respect to all other atoms has two components—(i) a pair potential description of each system and (ii) a many-body embedded atom method (EAM) contribution, using the model of Daw and Baskes [24]:

$$E_i = \frac{1}{2}\sum_j \phi_{\alpha\beta}(r_{ij}) - G_\alpha \left(\sum_j \sigma_\beta(r_{ij})\right)^{\frac{1}{2}} \quad (1)$$

where the pairwise interaction between two atoms i and j, separated by r_{ij}, is given by $\phi_{\alpha\beta}(r_{ij})$ (equation (2)) and has both long range electrostatic, $\phi_C(r_{ij})$ (equation (3)), and short range

contributions. The former are calculated using the Ewald method [25] with the particle–particle particle-mesh (PPPM) implementation of the method being adopted in order to improve computational efficiency [26]. The short range contributions are described using Morse, $\phi_M(r_{ij})$ (equation (4)), and Buckingham, $\phi_B(r_{ij})$ (equation (5)), potential forms [27, 28]. α and β are used to label the species of atom i and atom j respectively.

$$\phi_{\alpha\beta}(r_{ij}) = \phi_C(r_{ij}) + \phi_B(r_{ij}) + \phi_M(r_{ij}) \quad (2)$$

$$\phi_C(r_{ij}) = \frac{q_\alpha q_\beta}{4\pi\epsilon_0 r_{ij}} \quad (3)$$

$$\phi_M(r_{ij}) = D_{\alpha\beta}[\exp(-2\gamma_{\alpha\beta}(r_{ij} - r^0_{\alpha\beta})) - 2\exp(-\gamma_{\alpha\beta}(r_{ij} - r^0_{\alpha\beta}))] \quad (4)$$

$$\phi_B(r_{ij}) = A_{\alpha\beta}\exp\left(\frac{-r_{ij}}{\rho_{\alpha\beta}}\right) - \frac{C_{\alpha\beta}}{r_{ij}^6} \quad (5)$$

where $A_{\alpha\beta}, \rho_{\alpha\beta}, C_{\alpha\beta}, D_{\alpha\beta}, \gamma_{\alpha\beta}$ and $r^0_{\alpha\beta}$ are empirical parameters that describe the pair interactions between atom i and atom j. In comparison to the original CRG model [18] the updated version of the PuO$_2$ parameters [20] gives an improved description of the melting point of PuO$_2$ and is used here.

The second term in equation (1) uses the EAM to introduce a many-body perturbation to the pairwise interactions. The many-body dependence is achieved by summing a set of pairwise interactions, $\sum_j \sigma_\beta(r_{ij})$, and passing this through a non-linear embedding function: $\sigma_\beta(r_{ij})$ is inversely proportional to the 8th power of the inter-ionic separation (equation (6)) and a square root embedding function is used (equation (1)), where n_β and G_α are the respective constants of proportionality. The derivation of the parameters and a description of the functional terms used in the EAM component are given in [18, 20].

$$\sigma_\beta(r_{ij}) = \left(\frac{n_\beta}{r_{ij}^8}\right)\frac{1}{2}(1 + \text{erf}(20(r - 1.5))). \quad (6)$$

In order to prevent unrealistic forces occurring at short separations a short range cut-off using an error function is applied at 1.5 Å that reduces the EAM component gradually. This ensures that there is no discontinuity in the interatomic energy, which would arise from an abrupt cut-off.

Although the parameters for the actinide oxide systems have been developed previously, parameters must still be derived for the interactions of Xe and Kr with the actinide and oxygen species. A detailed description of this fitting procedure follows in section 2.2. Due to Xe and Kr being inert gases, the interactions with host cation and oxygen ions were adequately described with the purely pairwise Buckingham potential (equation (5)), with no many-body description being necessary. Note also that the gas–gas interactions used here were developed previously by Tang–Toennies [29], enabling mixed gas Xe–Kr systems to be studied.

2.2. Fitting proceedure

The fitting procedure for gas interactions with the host actinide oxide is conducted over three stages: (i) firstly structure
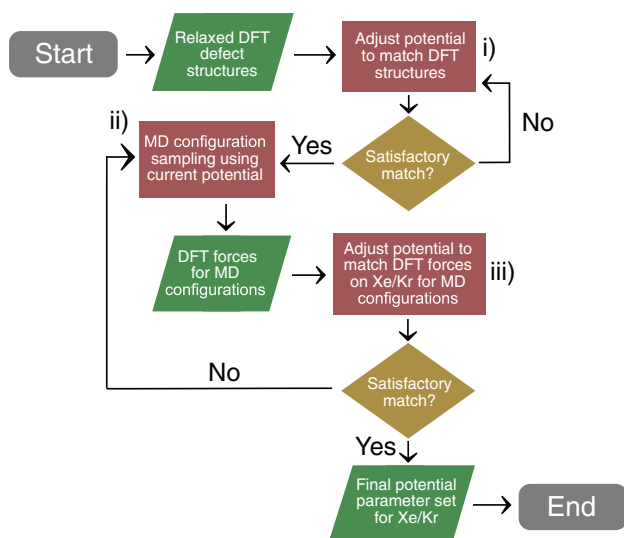
Figure 1. A schematic illustration of the fitting procedure conducted for the development of the potential parameters for Xe and Kr in CeO$_2$, ThO$_2$, UO$_2$ and PuO$_2$. The final parameter set is reported in table 4.

matching is carried out to DFT energy minimised Xe/Kr defects in CeO$_2$, ThO$_2$, UO$_2$ and PuO$_2$ to develop an initial set of potential parameters, (ii) using this initial attempt, structures are generated using MD for Xe or Kr at a bound Schottky trio in CeO$_2$, ThO$_2$, UO$_2$ and PuO$_2$ at temperatures of 300 K, 1500 K, 3000 K and 5000 K (at which temperature the structure is liquid) to ensure a significant sample of representative configurations and, finally, (iii) the potential parameters are readjusted to reproduce the forces on Xe and Kr predicted by DFT for these MD configurations. Stages (ii) and (iii) can be repeated using updated parameters until a satisfactory match is achieved. This procedure is illustrated in figure 1 with stages (i)–(iii) labelled and the final parameter set is reported in section 3.2. This approach aims to include insight from DFT on the temperature effects of fission gas behaviour, while avoiding computationally expensive DFT-MD calculations. In line with the fitting approach used for the actinide oxides [18], the ρ parameters are scaled to the ionic radii of the actinides involved. Gas-oxygen interactions are kept the same for all systems to enable the possibility of modelling Xe and Kr in mixed oxides. Gas–gas interations were not fitted here and the potential developed by Tang–Toennies [29] has been used throughout.

For the generation of MD configurations, calculations were carried out on $2 \times 2 \times 2$ fluorite supercells so that subsequent DFT force calculations were manageable. An NVT ensemble was used with a thermostat relaxation time of 0.1 ps at 300 K, 1500 K, 3000 K and 5000 K and a timestep of 2 fs.

2.3. DFT details

DFT calculations were carried out using with the plane-wave Vienna *ab initio* simulation package (VASP) [30] with standard projected augmented wave (PAW) pseudo-potentials [31]. The exchange correlation term was modelled using the generalised gradient approximation (GGA) of Perdew, Burke and Ernzeroff (PBE) [32]. A consistent plane wave cut off of

Table 1. The values of U and J as well as the method used in this study for each oxide.

Phase	Method	$U(M_f)$	$J(M_f)$	$U(O_f)$	$J(O_f)$
CeO$_2$	Dudarev [36]	5.00	—	5.50	—
ThO$_2$	Lichtenstein [35]	4.50	0.50	—	—
UO$_2$	Lichtenstein [35]	4.50	0.51	—	—
PuO$_2$	Lichtenstein [35]	4.50	0.50	—	—

500 eV was used throughout. The magnetic ordering of UO$_2$ was described with the 1k antiferromagnetic ordering [33, 34]. CeO$_2$ and ThO$_2$ were maintained as non-magnetic, while PuO$_2$ was magnetic. In order to describe the behaviour of the localised cation f states the orbital-dependent, Coulomb potential, U, and the exchange parameter J were used within DFT + U [35, 36]. The values of U and J for each oxide were taken from established literature data [37–40] and are summarised in table 1. To include van der Waals (vdW) interactions the pairwise interactions of Grimme [41] are implemented. To avoid metastable states U-ramping was applied to the perfect supercell in advance of the defect calculations [42]. For all calculations a $2 \times 2 \times 2$ fluorite supercell was used, with $2 \times 2 \times 2$ Monkhorst–Pack k-point mesh. Gaussian smearing of bands was performed with a broadening width of 0.1 eV. Geometry relaxation of internal coordinates was achieved until the energy differences between two consecutive steps was below 1×10^{-4} eV, or all forces were less then 1×10^{-2} eV Å^{-1}. The convergence criteria were selected on the basis that it would be difficult to fit an empirical potential to DFT forces with greater accuracy than this.

A single gas atom was used as the reference energy for the calculation of gas incorporation energies. As the only defect reactions considered maintain the charge on the supercell, it was not necessary to correct for interactions between the defect and the charge compensating background. Any such correction would cancel out (see reactions (7)–(10)).

3. Results and discussion

3.1. DFT defect energies

To generate defect structures for the initial stage of the fitting procedure energy minimisation calculations were carried out for Xe and Kr accommodation at a number of sites in CeO$_2$, ThO$_2$, UO$_2$ and PuO$_2$. The energies for Xe or Kr incorporation into an interstitial site (reaction (7)), an oxygen vacancy (reaction (8)), a cation vacancy (reaction (9)) and a bound Schottky trio (reaction (10)) are reported for CeO$_2$, ThO$_2$, UO$_2$ and PuO$_2$ (see table 2):

$$X \rightarrow X_i \tag{7}$$

$$X + V_O^{\bullet\bullet} \rightarrow X_O^{\bullet\bullet} \tag{8}$$

$$X + V_M'''' \rightarrow X_M'''' \tag{9}$$

$$X + \{V_M'''' : 2V_O^{\bullet\bullet}\}^\times \rightarrow \{X_{M:2O}^\times\}^\times \tag{10}$$

where reactions (7)–(10) use Kröger–Vink notation [43]. M and X represent the cation and gas species respective. Three Schottky trio cluster configurations were considered, whereby both oxygen

Table 2. DFT incorporation energies for Xe and Kr into the actinide oxides MO_2 (where M is Ce, Th, U or Pu). The resultant defect structures are used in fitting the empirical potential.

	CeO_2 (eV)	ThO_2 (eV)	UO_2 (eV)	PuO_2 (eV)
$Xe_i^\times$	10.56	10.19	8.94	10.70
Xe_M''''	4.71	3.74	3.70	5.01
$Xe_O^{\bullet\bullet}$	7.68	7.50	6.85	8.80
$Xe_{M:2O}^\times$	0.72	0.32	0.49	0.87
$Kr_i^\times$	7.48	6.96	6.15	7.46
Kr_M''''	3.31	2.64	2.49	2.66
$Kr_O^{\bullet\bullet}$	5.00	4.84	4.56	5.92
$Kr_{M:2O}^\times$	0.28	0.11	0.18	0.39

Table 3. DFT incorporation energies for Xe in UO_2 at different sites from literature data [44–46].

	Geng (eV) [44]	Thompson (eV) [45]	Nerikar (eV) [46]
$Xe_i^\times$	9.75	9.73	11.11
Xe_U''''	—	—	2.5
$Xe_O^{\bullet\bullet}$	—	—	9.50
$Xe_{U:2O}^\times$	0.18	1.06	1.38

vacancies occupy first nearest neighbour positions with respect to the uranium vacancy and occupy either first (SD1), second (SD2) or third (SD3) nearest neighbour positions with respect to each other. For all incorporation energies into Schottky trios, the oxygen vacancy positions are allowed to reconfigure, such that the lowest energy configuration with (RHS reaction (10)) or without a gas atom (LHS reaction (10)) is always used. Table 2 shows that for Xe and Kr incorporation into all of the host systems, the lowest energies are predicted for the bound Schottky trio. The interstitial is the least favourable incorporation site, while incorporation at the cation site is more favourable than the oxygen site for all systems. Chemical interactions associated with the coordination environment of a given site are limited due to the noble gases being inert. Consequently, the lower incorporation energies can be understood in terms of a steric argument and are associated with defects that present a larger space to accommodate the relatively large Xe and Kr atoms. Similarly, host systems with larger lattice parameters also present a greater volume for more favourable incorporation of Xe and Kr. By comparison with literature data [44–46] reported in table 3 for Xe in UO_2 similar trends can be seen, whereby low incorporation energies are predicted in the bound Schottky trio. The DFT data from Nerikar *et al* [46] further supports that incorporation is more favourable at a uranium site than an oxygen site.

3.2. Fitting results

The initial set of gas parameters was iteratively refined by minimising the atomic forces predicted by the potential when using the DFT defect structures calculated in section 3.1. The empirical interatomic forces were converged to within 0.066 eV $Å^{-1}$ and 0.055 eV $Å^{-1}$ per atom against the DFT forces (in this case zero) for Xe and Kr defects respectively. MD configurations from 300 K to 5000 K were sampled using this initial parameter set and then DFT atomic forces were calculated using those structures. Finally, the potential set was further refined to reproduce the DFT force acting on Xe or Kr in each of the MD generated structures. Forces on the host lattice were omitted from fitting due to the differences between the DFT and empirical descriptions being used (e.g. slight differences in the predicted lattice parameter). Forces on Xe and Kr were refined on average to within 0.251 eV $Å^{-1}$ and 0.224 eV $Å^{-1}$ of the DFT forces respectively.

Table 4 reports the final parameter set derived for Xe–O, Xe–Ce, Xe–Th, Xe–U, Xe–Pu, Kr–O, Kr–Ce, Kr–Th, Kr–U and Kr–Pu. These parameters were derived in conjunction with the gas–gas interactions of Tang–Toennies [29] to allow mixed gas calculations. Further validation may be necessary if one wishes to use the potentials derived here with alternative gas–gas interactions.

The potentials reported in table 4 are plotted as a function of gas-ion separation in figure 2. It can be seen that the potentials predict less repulsion at small separation for Kr than for Xe, this would be expected based on the smaller atomic radius of Kr compared to that of Xe [47]. Similarly, interactions between a given gas atom and cations are ordered based on cation radius, in that greater repulsion corresponds greater radii. For example, the radius of Th is greatest (1.05 Å) and that of Pu the least (0.96 Å) in line with the tends shown in figure 2. Interactions between gas atoms and oxygen anions are predicted to act over a longer range and be softer than the interactions with the small hard cations. Again this is expected given the large (1.42 Å) and highly polarisable nature of O. These trends intuitively make sense and provide reassurance that the parameter set is sensible.

Figure 3 shows the relaxed defect structures for Xe and Kr in the SD1 defect for the $2 \times 2 \times 2$ (DFT and empirical potential) and $10 \times 10 \times 10$ (empirical potential only) UO_2 supercells. The displacements of host atoms due to the incorporation of Xe and Kr are represented by the color gradient. It can be seen that in all cases, regardless of supercell size, there is agreement that the most displaced atoms are the first nearest neighbour oxygen ions. For the $2 \times 2 \times 2$ supercell the empirical potential exhibits smaller displacements for ions beyond the first nearest neighbour positions. This may be due to the atoms in one cell experiencing the displacement field from the surrounding cells. This was examined by calculating the displacement due to gas incorporation in the $10 \times 10 \times 10$ UO_2 supercell. Here it can been seen that greater displacement is predicted for atoms beyond the first nearest neighbour sites compared to the $2 \times 2 \times 2$ supercell, giving better agreement with the DFT results. The displacement field around the gas atom remains symmetrical, as expected from the centro-symmetric Buckingham potential used here combined with the symmetry of the defect.

3.3. Validation of empirical parameters

Although the agreement with force matching between DFT and the potential using static and MD based structures has been discussed, it is necessary to test the potential's predictive

Table 4. Potential parameters for Xe and Kr in CeO$_2$, ThO$_2$, UO$_2$ and PuO$_2$ of the Buckingham potential form given by equation (5).

	Xe–O	Xe–Ce	Xe–Th	Xe–U	Xe–Pu
$A_{\alpha\beta}$ (eV)	1877.5990	6308.6510	6238.0739	6606.3980	6591.3310
$\rho_{\alpha\beta}$ (Å)	0.340 1910	0.289 1647	0.313 0134	0.298 1080	0.286 1837
$C_{\alpha\beta}$ (eV Å^6)	46.478 139	18.013 067	20.013 067	19.013 067	18.013 067
	Kr–O	Kr–Ce	Kr–Th	Kr–U	Kr–Pu
$A_{\alpha\beta}$ (eV)	1862.8460	7885.8137	7797.5924	8257.9975	8239.1637
$\rho_{\alpha\beta}$ (Å)	0.323 1814	0.274 7064	0.297 3627	0.283 2030	0.271 8745
$C_{\alpha\beta}$ (eV Å^6)	39.908 723	17.112 414	19.012 431	18.062 414	17.112 414

Note: Note that Coulombic, Morse and EAM potentials were not used for the gas potentials.
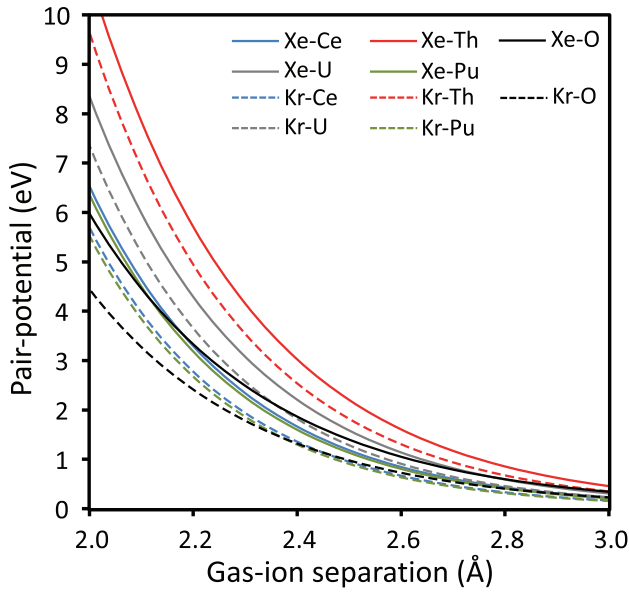
Figure 2. The pair-potential interactions plotted as a function of gas-ion separation for Xe–O, Xe–Ce, Xe–Th, Xe–U, Xe–Pu, Kr–O, Kr–Ce, Kr–Th, Kr–U and Kr–Pu. Expanded views of the potential are shown near the oxygen-gas separation, the cation-gas separation and the potential minima.

Figure 3. The displacement of U and O atoms due the incorporation of (a) Kr and (b) Xe into a pre-existing Schottky defect. The color of the U and O atoms corresponds to the magnitude of the displacement. Xe and Kr atoms are shown by grey and beige spheres respectively and are marked with a black cross.

capabilities by comparing against properties not used during fitting. When calculating the incorporation energies in table 2 reference energies must be used for the gas species outside of the host lattice. As there are no equivalent reference states when using the empirical potential, it is necessary to validate the potential against DFT for reactions that negate such reference states. Validation was, therefore, carried out against the trapping energy of a gas interstitial with vacancy accommodation sites in CeO$_2$, ThO$_2$, UO$_2$ and PuO$_2$. As neither the products nor reactants in these reactions involve any species outside the host lattice, the issue of reference energies is removed so that the DFT and empirical potential energies are directly equivalent. The potentials are validated for gas interstitial trapping with an oxygen vacancy (reaction (11)), a cation vacancy (reaction (12)) and a bound Schottky trio (reaction (13)).
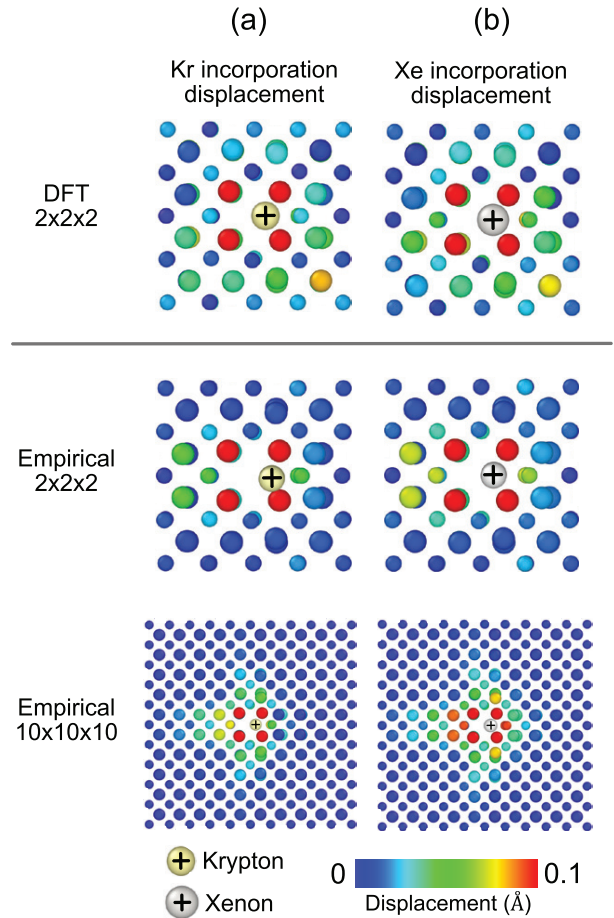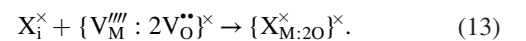
$$X_i^\times + V_O^{\bullet\bullet} \rightarrow X_O^{\bullet\bullet} \tag{11}$$

$$X_i^\times + V_M^{''''} \rightarrow X_M^{''''} \tag{12}$$

$$X_i^\times + \{V_M^{''''} : 2V_O^{\bullet\bullet}\}^\times \rightarrow \{X_{M:2O}^\times\}^\times. \tag{13}$$

The trapping energies associated with these reactions are given in figure 4 for the new empirical potential (parameters reported in table 4) and for DFT using the incorporation energies calculated in section 3.1 (see table 2). Where possible, comparison has also been made to literature UO$_2$ DFT results [14, 44–46]. Figure 4 shows similar trends for the trapping
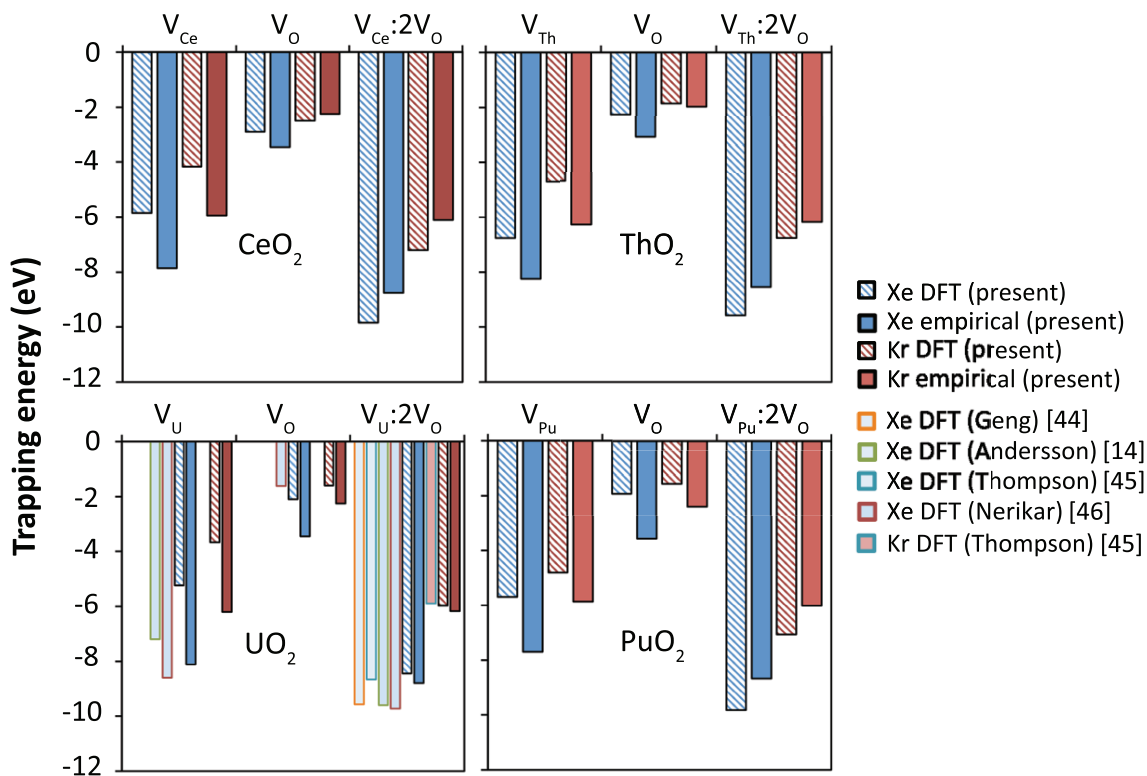
Figure 4. The trapping energy for the incorporation of a Xe (blue) or Kr (red) atom starting at the interstitial site into an oxygen vacancy (reaction (11)), cation vacancy (reaction (12)) or Schottky defect (reaction (13)). DFT results (partially filled columns) are reported from the literature [14, 44–46] and the present study (using table 2) for comparison with the new empirical potential potential (solid columns).
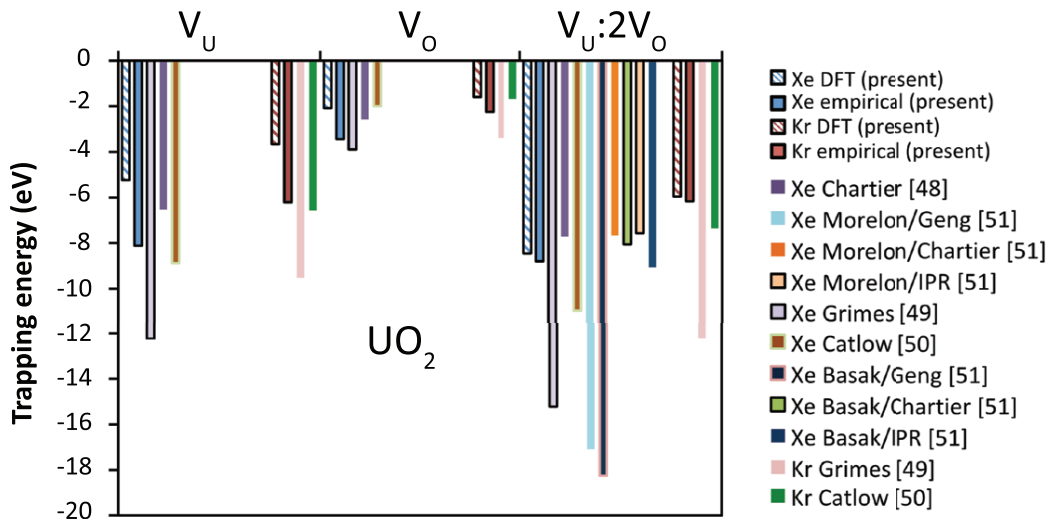

Figure 5. The trapping energy for the incorporation of a Xe or Kr atom starting at the interstitial site into an oxygen vacancy (reaction (11)), uranium vacancy (reaction (12)) or Schottky defect (reaction (13)). DFT results (partially filled columns) are reported from the present study (using table 2) for comparison with the new empirical potential potential and a range of alternative empirical potentials (solid columns).

energies for Xe and Kr defects in CeO$_2$, ThO$_2$, UO$_2$ and PuO$_2$ between the empirical potential and the DFT methods used in this paper. Additionally, for UO$_2$ the empirical values lie within the scatter shown by literature DFT data. The origin

of variation in DFT values may lie in the different methods implemented (e.g. LDA versus GGA). For all cases trapping energies are less negative for Kr than Xe regardless of the system studied. This is expected as Xe has a greater atomic

radius than Kr and it is, therefore, expected to exhibit stronger (more negative) trapping energies to vacancy defects, which provide more space relative to the interstitial site. Similarly, Xe and Kr both exhibit the most negative (strongest) trapping energies with the Schottky defect across all host systems, due to the large volume presented by this defect. Figure 5 shows the trapping energy predicted by a number of empirical potentials. These were determined using the incorporation energy results published in the literature [48–51]. These were calculated using the UO_2 and Xe/Kr potentials of Chartier *et al* [48], Grimes [49] and Catlow [50]. Additionally, Thompson *et al* [51] used the the Basak [52] or Morelon [53] UO_2 potentials in combination with the Xe potential of Geng *et al* [54] and Chartier *et al* [48] as well as their own genetic algorithm iterative potential refinement (IPR) approach [51]. For Kr the new empirical potential reported here performs better than the Grimes and Catlow potentials for trapping into the cation and Schottky trio defects. The Catlow potential compares marginally better than the new potential for Kr trapping into the oxygen vacancy, although this is the least thermodynamically important (least stable) trapping site. The lowest energy trapping site for Xe is predicted to be the bound Schottky trio for all empirical potentials reported here. The new Xe potential compares favourable with DFT trapping energies, in particular for the important bound Schottky trio.

4. Conclusions

Understanding the behaviour of fission gases in nuclear fuel is crucial for the safe and efficient operation of nuclear reactors. Atomistic simulations provide a useful tool for investigating the underlying mechanisms that govern fission gas behaviour. As such, empirical potentials, which the simulations rely upon, are continuously improved. To this end we have developed a set of Xe and Kr Buckingham potentials for use with the many-body CRG potential, which was shown to more accurately describe the thermophysical properties of actinide oxides and their solid solutions from 300 K to 3000 K. Fitting was carried out by force matching to DFT using MD generated configurations of Xe and Kr in CeO_2, ThO_2, UO_2 and PuO_2 at 300 K, 1500 K, 3000 K and 5000 K. This ensures the potentials provide a reasonable description of Xe and Kr interactions with the host systems for coordination environments relevant to the wide range of temperatures experienced by nuclear fuel. The potential set is validated against literature and newly presented DFT trapping energies for an interstitial gas atom being accommodated into cation, oxygen and bound Schottky trios. The potential parameter set creates the possibility of investigating Xe and Kr in CeO_2, ThO_2, UO_2 and PuO_2 including solid solutions of these end members.

Acknowledgments

References

[1] Kim Y-E, Park J-W and Cleveland J 2006 Thermophysical properties database of materials for light water reactors and heavy water reactors IAEA-TECDOC-1496, International Atomic Energy Agency
[2] Olander D 2009 *J. Nucl. Mater.* **389** 1–22
[3] Matzke H 1980 *Radiat. Eff.* **53** 219–42
[4] Une K and Kashibe S 1990 *J. Nucl. Sci. Technol.* **27** 1002–16
[5] White R J and Tucker M O 1983 *J. Nucl. Mater.* **118** 1–38
[6] Tonks M R, Liu X-Y, Andersson D A, Perez D, Chernatynskiy A, Pastore G, Stanek C R and Williamson R 2016 *J. Nucl. Mater.* **469** 89–98
[7] Popov S G, Ivanov V K, Carbajo J J and Yoder G L 2000 Thermophysical properties of MOX and UO_2 fuels including the effects of irradiation *ONRL Report* ORNL/TM-2000/351, Oak Ridge National Laboratory
[8] Lee W E, Gilbert M, Murphy S T and Grimes R W 2013 *J. Am. Ceram. Soc.* **96** 2005–30
[9] Sokolov F, Kukuda K and Nawada H P 2005 Thorium fuel cycle—potential benefits and challenges IAEA-TECDOC-1450, International Atomic Energy Agency
[10] Park Y S, Kolman D G, Ziraffe H, Haertling C and Butt D P 1999 *MRS Proc.* **556** 129–34
[11] Nelson A T, Rittman D R, White J T, Dunwoody J T, Kato M and McClellan K J 2014 *J. Am. Ceram. Soc.* **97** 3652–9
[12] Turnbull J A, Friskney C A, Findlay J R, Johnson F A and Walter A J 1982 *J. Nucl. Mater.* **107** 168–84
[13] Nerikar P V, Parfitt D C, Casillas Trujillo L A, Andersson D A, Unal C, Sinnott S B, Grimes R W, Uberuaga B P and Stanek C R 2011 *Phys. Rev.* B **84** 174105
[14] Andersson D A, Uberuaga B P, Nerika P V, Unal C and Stanek C R 2011 *Phys. Rev.* B **84** 054105
[15] Turnbull J A 1971 *J. Nucl. Mater.* **38** 203–12
[16] Schwen D, Huang M, Bellon P and Averback R S 2009 *J. Nucl. Mater.* **392** 35–9
[17] Parfitt D C and Grimes R W 2009 *J. Nucl. Mater.* **392** 28–34
[18] Cooper M W D, Rushton M J D and Grimes R W 2014 *J. Phys.: Condens. Matter* **26** 105401
[19] Cooper M W D, Murphy S T, Fossati P C M, Rushton M J D and Grimes R W 2014 *Proc. R. Soc.* A **470** 20140427
[20] Cooper M W D, Murphy S T, Rushton M J D and Grimes R W 2015 *J. Nucl. Mater.* **461** 206–14
[21] Gale J D 1997 *J. Chem. Soc. Faraday Trans.* **93** 629–37
[22] Plimpton S 1995 *J. Comput. Phys.* **117** 1–19
[23] Todorov I T, Smith W, Trachenko K and Dove M T 2006 *J. Mater. Chem.* **16** 1911–8
[24] Daw M S and Baskes M I 1984 *Phys. Rev.* B **29** 6443–53
[25] Ewald P P 1921 *Ann. Phys.* **369** 253–87
[26] Hockney R W and Eastwood J W 1988 *Computer Simulation Using Particles* (Bristol, PA: Taylor and Francis)
[27] Morse P 1929 *Phys. Rev.* **34** 57–64

[28] Buckingham R A 1938 *Proc. R. Soc.* A **168** 264–83
[29] Tang K T and Toennies J P 2003 *J. Chem. Phys.* **118** 4976–83
[30] Kresse G and Furthmüller J 1996 *Phys. Rev.* B **54** 11169–86
[31] Kresse G and Joubert D 1999 *Phys. Rev.* B **59** 1758–75
[32] Perdew J P, Burke K and Ernzerhof M 1996 *Phys. Rev. Lett.* **77** 3865
[33] Dorado B, Freyss M, Amadon B, Bertolus M, Jomard G and Garcia P 2013 *J. Phys.: Condens. Matter* **25** 333201
[34] Dorado B and Garcia P 2013 *Condens. Matter Phys.* **87** 18–20
[35] Lichtenstein A I, Anisimov V I and Zaanen J 1995 *Phys. Rev.* B **52** R5467
[36] Dudarev S L, Botton G A, Savrasov S Y, Humphreys C J and Sutton A P 1998 *Phys. Rev.* B **57** 1505
[37] Keating P R L, Scanlon D O, Morgon B J, Galea N M and Watson G W 2012 *J. Phys. Chem.* C **116** 2443–52
[38] Sevik C and Çağun T 2009 *Phys. Rev.* B **80** 014108
[39] Dorado B, Jomard G, Freyss M and Bertolus M 2010 *Phys. Rev.* B **82** 035114
[40] Wang H and Konashi K 2012 *J. Alloys Compd.* **533** 53–7
[41] Grimme S 2006 *J. Comput. Chem.* **27** 1787–99
[42] Meredig B, Thompson A, Hansen H A and Wolverton C 2010 *Phys. Rev.* B **82**

[43] Kröger F A and Vink H J 1956 *Solid State Phys.* **3** 307–435
[44] Geng H Y, Chen Y, Kaneta Y, Motoyasu K and Wu Q 2010 *Phys. Rev.* B **82** 094106
[45] Thompson A E and Wolverton C 2011 *Phys. Rev.* B **84** 134111
[46] Nerikar P, Liu X-Y, Uberuaga B P, Stanek C R and Sinnott S B 2009 *J. Phys.: Condens. Matter* **21** 1–11
[47] Shannon R D 1976 *Acta Crystallogr.* A **32** 751
[48] Chartier A, Van Brutzel L and Freyss M 2010 *Phys. Rev.* B **81** 17411
[49] Grimes R W 1990 Simulating the behaviour of inert gases in UO$_2$ UKAEA *Harwell Laboratory Report* AEA-In-Tec-0195, Atomic Energy Agency
[50] Catlow C R A 1978 *Proc. R. Soc.* A **364** 473–97
[51] Thompson A E, Meredig B and Wolverton C 2014 *J. Phys.: Condens. Matter* **26** 105501
[52] Basak C B, Sengupta A K and Kamath H S 2003 *J. Alloys Compd.* **360** 210–6
[53] Morelon N-D, Ghaleb D, Delaye J-M and Van Brutzel L 2003 *Phil. Mag.* **83** 1533–55
[54] Geng H Y, Chen Y, Kaneta Y and Kinoshita M 2008 *J. Alloys Compd.* **457** 465–71